ACS OMEGA

Open Access

http://pubs.acs.org/journal/acsodf

Article

Polymeric Backbone Eutectogel Electrolytes for High-Energy Lithium-Ion Batteries

An-Sofie Kelchtermans,* Bjorn Joos, Dries De Sloovere, Andreas Paulus, Jonas Mercken, Satish Kumar Mylavarapu, Ken Elen, Wouter Marchal, Alexander Tesfaye, Travis Thompson, Marlies K. Van Bael, and An Hardy*

Cite This: *ACS Omega* 2023, 8, 36753−36763

Read Online

ACCESS | Metrics & More | Article Recommendations | Supporting Information

ABSTRACT: This work introduces a polymeric backbone eutectogel (P-ETG) hybrid solid-state electrolyte with an *N*-isopropylacrylamide (NIPAM) backbone for high-energy lithium-ion batteries (LIBs). The NIPAM-based P-ETG is (electro)chemically compatible with commercially relevant positive electrode materials such as the nickel-rich layered oxide $LiNi_{0.6}Mn_{0.2}Co_{0.2}O_2$ (NMC622). The chemical compatibility was demonstrated through (physico)chemical characterization methods. The nonexistence (within detection limits) of interfacial reactions between the electrolyte and the positive electrode, the unchanged bulk crystallographic composition, and the absence of transition metal ions leaching from the positive electrode in contact with the electrolyte were demonstrated by Fourier transform infrared spectroscopy, powder X-ray diffraction, and elemental analysis, respectively. Moreover, the NIPAM-based P-ETG demonstrates a wide electrochemical stability window (1.5−5.0 V vs Li^+/Li) and a reasonably high ionic conductivity at room temperature (0.82 mS cm^{-1}). The electrochemical compatibility of a high-potential NMC622-containing positive electrode and the P-ETG is further demonstrated in Li|P-ETG|NMC622 cells, which deliver a discharge capacity of 134, 110, and 97 mAh g^{-1} at C/5, C/2, and 1C, respectively, after 90 cycles. The Coulombic efficiency is >95% at C/5, C/2, and 1C. Hence, gaining scientific insights into the compatibility of the electrolytes with positive electrode materials that are relevant to the commercial market, like NMC622, is important because this requires going beyond the electrolyte design itself, which is essential to their practical applications.

INTRODUCTION

The fast depletion of nonrenewable fossil fuels and related environmental issues, such as global warming and air pollution, necessitate the replacement of gasoline in automotive applications.[1−3] Lithium-ion batteries (LIBs) have advanced into this field, both in pure and hybrid electric vehicles, due to their high gravimetric and volumetric energy density.[4,5] To compete with combustion engines, LIBs for automotive applications should provide large specific energy densities to deliver a driving range of more than 500 km, combined with fast charging times.[6] The battery's specific energy has already improved from 110 W h kg^{-1} in 2010 to 250 W h kg^{-1} in 2020. It is expected that it will further improve up to 450 W h kg^{-1} by 2030 by introducing new battery materials.[7]

A positive electrode material showing a high energy density is a prerequisite for performant LIBs, as it directly participates in electrochemical reactions and plays an important role in determining the practical energy storage capability. It is well-known that layered $LiCoO_2$, one of the traditional LIB cathode materials, has a limited energy density of ∼140 mA h g^{-1} (∼500 W h kg^{-1}) at the upper cutoff voltage of 4.2 V vs Li^+/Li.[8,9] Alternatively, layered oxides with the composition $LiNi_xMn_yCo_zO_2$ (NMCxyz) have attracted much attention as positive electrode materials because of their high specific capacity.[10] Different NMC compositions with various electrochemical characteristics, such as NMC111,[11] NMC622,[12] and NMC811,[13] have been developed.[14] Increasing the nickel content results in higher capacities as nickel, via the $Ni^{4+/3+/2+}$ redox couples, is the main active redox species in the structure.[15] Therefore, nickel-rich NMCxyz cathode materials ($x > 0.5$), such as NMC622 and NMC811, are of great interest in developing high-energy-density batteries. However, increasing the nickel content also decreases the thermal stability, resulting in thermal runaway if a flammable conventional organic liquid electrolyte is employed in the battery.[16,17] Therefore, to improve the energy density and safety of LIBs, solid-state electrolytes were introduced instead.

The development of solid-state electrolytes with high ionic conductivity and a broad electrochemical stability window while showing thermal and mechanical stability has recently drawn significant attention.[18−27] Several sufficiently to very highly ionic conductive electrolyte materials have been identified.[25−27] Solid composite electrolytes are the focus of the work at hand. They are composed of a liquid lithium-ion conducting electrolyte enclosed within a solid backbone. Examples are ionogels in which an ionic liquid is confined within silica-derived networks.[25] Such electrolytes have been

Received: May 4, 2023
Accepted: September 5, 2023
Published: September 26, 2023

considered promising candidates for solid-state LIBs as they allow a high ionic conductivity combined with the rigidity of a solid, having low vapor pressure.[25,28,29] Joos et al.[30] introduced a polymeric backbone eutectogel (P-ETG) as a hybrid solid-state electrolyte in which a lithium-ion-conducting deep eutectic solvent (DES) is confined within a 4-acryloyl morpholine (ACMO)-based polymeric backbone. DESs share many properties with ionic liquids such as low vapor pressure and nonflammability. However, they can have additional advantages such as ease of synthesis and low cost of their components.[31,32] Compared to their silica-based eutectogel counterparts,[33] the P-ETGs can be efficiently processed from liquid precursors through UV curing. Furthermore, they generally possess good mechanical flexibility, allowing for good interfacial contact with the electrodes. The P-ETGs have good electrochemical stability (up to 4.5 V vs Li^+/Li), sufficient ionic conductivity up to 0.78 mS cm^{-1}, and stable cycling results of Li|P-ETG|$LiFePO_4$ cells.[30]

Given the availability of these interesting candidate materials, the bottleneck of solid-state battery development today is no longer maximizing the ionic conductivity. The main issue now has shifted toward integrating the solid-state electrolyte and electrodes.[34] Controlling the properties of the electrode−electrolyte interface and maintaining chemical and mechanical stability between the electrodes and the solid-state electrolyte during battery operation are the challenges of cell integration. During cycling, a good interface between a solid electrolyte and an electrode necessitates quick ion transport, an ideal contact area, and chemical stability.[35] However, it was discovered through experiments that the ACMO backbone units in the reported[30] P-ETG have limited chemical stability when they come into contact with high-potential positive electrode materials like NMC622.

By modification of the polymer backbone, the current work aims to improve the stability of P-ETGs when in contact with high-voltage positive electrode materials. *N*-Isopropylacrylamide (NIPAM) was successfully used to replace the ACMO backbone, exhibiting intriguing ionic conductivity, a wide electrochemical stability window, and high thermal stability. NIPAM was selected because it does not contain any ether functions, which we hypothesized to be responsible for limiting the cycle life in combination with high-energy, positive electrodes. Charging the ACMO backbone to high voltages (4.2−4.3 V vs Li^+/Li) causes fast capacity loss and short cycle life, similar to common liquid electrolytes that include ether functionalities.[36−38] Also, the most common solid polymer electrolyte, PEO (poly(ethylene oxide), has an anodic stability that is limited to potentials around 4.0 V vs Li^+/Li.[39]

As a result, the challenge of electrode−electrolyte integration is the primary focus of this work, which employs the NIPAM-based P-ETG electrolyte and NMC622 as representative high-potential positive electrode materials. Obtaining scientific insights into the compatibility of the P-ETG electrolyte with commercially relevant positive electrode materials, such as NM6622, is crucial because this necessitates taking additional steps beyond electrolyte design, bridging the gap between academic research and industry. In addition to electrochemical impedance spectroscopy (EIS), (physico)-chemical characterization techniques like Fourier transform infrared (FT-IR) spectroscopy, powder X-ray diffraction (PXRD), and inductively coupled plasma-atomic emission spectroscopy (ICP-AES) are used to investigate the electrochemical compatibility between the positive electrode and the electrolyte. At a variety of charge−discharge rates (C-rates), the galvanostatic cycling behavior of Li|P-ETG|NMC622 cells is evaluated.

EXPERIMENTAL SECTION

Chemicals. Bis(trifluoromethane)sulfonimide lithium salt (LiTFSI, 99.9% trace metal basis) and *N*-methylacetamide (MAc, ≥99%) were purchased from Sigma-Aldrich. MAc was dried using molecular sieves (3 Å, 4−8 mesh, Acros) for 72 h at 45 °C, while the LiTFSI was dried in a vacuum oven for 72 h at 110 °C to remove traces of water. These materials were stored in a nitrogen-filled glovebox with controlled oxygen and water content (H_2O < 0.1 ppm, O_2 < 0.1 ppm, MBRAUN). The initiator 2,2-dimethoxy-2-phenyl acetophenone (DMPA, 99%, pure, stabilized, Acros) was used as received. NIPAM (99%, pure, stabilized, Acros) and ethylene glycol dimethacrylate (EGDMA, TCI, >97.0%) were disinhibited over a column of activated basic alumina before use.

Preparation of P-ETG Electrolytes. The DES was prepared according to a procedure reported by Boisset et al.[40,41] LiTFSI and MAc were mixed in a 1:4 molar ratio with vigorous stirring at 40 °C in a nitrogen-filled glovebox (H_2O < 0.1 ppm, O_2 < 0.1 ppm, MBRAUN) until a homogeneous transparent liquid was obtained. The synthesis of P-ETG was similar to that described in our group's previous work.[30] The polymeric backbone precursor consisted of a mixture of the hydrophilic NIPAM monomer, a cross-linker (ethylene glycol dimethacrylate, EGDMA), and a photoinitiator (DMPA), with a (monomer/cross-linker)/initiator molar ratio of (90:10):5. After obtaining a homogeneous mixture in ambient air, nitrogen was bubbled through the precursor solution to remove dissolved oxygen and the solution was subsequently introduced in the nitrogen-filled glovebox. The P-ETGs were prepared by homogeneously mixing the desired volumes of DES and polymeric backbone precursor, and the mixture was stirred to obtain a homogeneous blend. These solutions were hermetically enclosed between two glass substrates separated by 1 mm spacers and transferred out of the glovebox for polymerization. The polymerization was performed by means of UV illumination (365 nm) for 1 h. The obtained P-ETGs were subsequently transferred into an argon-filled glovebox with a controlled atmosphere (H_2O < 0.1 ppm, O_2 < 0.6 ppm, MBRAUN).

Characterization. *(Physico)chemical Characterization.* PXRD (Bruker D8 diffractometer, Cu Kα radiation) was carried out for the phase identification of NMC622. The P-ETGs were analyzed by means of attenuated total reflection-Fourier transform infrared spectroscopy (ATR-FT-IR, PerkinElmer Frontier, 32 scans, scan range 4000−400 cm^{-1}, resolution 4 cm^{-1}) at room temperature. The MIRacle single reflection ATR accessory was used to allow measurement in the absence of a KBr salt. The DES, on the one hand, and Ni, Co, and Mn 1000 ppm standards (Merck multi-element standard IV), on the other hand, were diluted with 5% HNO_3 to the 5 ppb−100 ppm range, and 0.05−0.1−0.5−1−2−5−10−50−100 ppm concentrations, respectively, for ICP-AES measurements. Raman spectra were acquired on a Horiba Jobin-Yvon T64000 spectrometer, equipped with a Symphony detector and a long working distance 100x Olympus objective. The 488 nm Lexel SHG laser was operated at a power of less than 20 mW. Sample preparation comprised sealing the P-ETG between a microscope slide and a cover glass with vacuum grease in a dry room (dew point of −45 °C). Thermogravi-

https://doi.org/10.1021/acsomega.3c03081
ACS Omega 2023, 8, 36753−36763

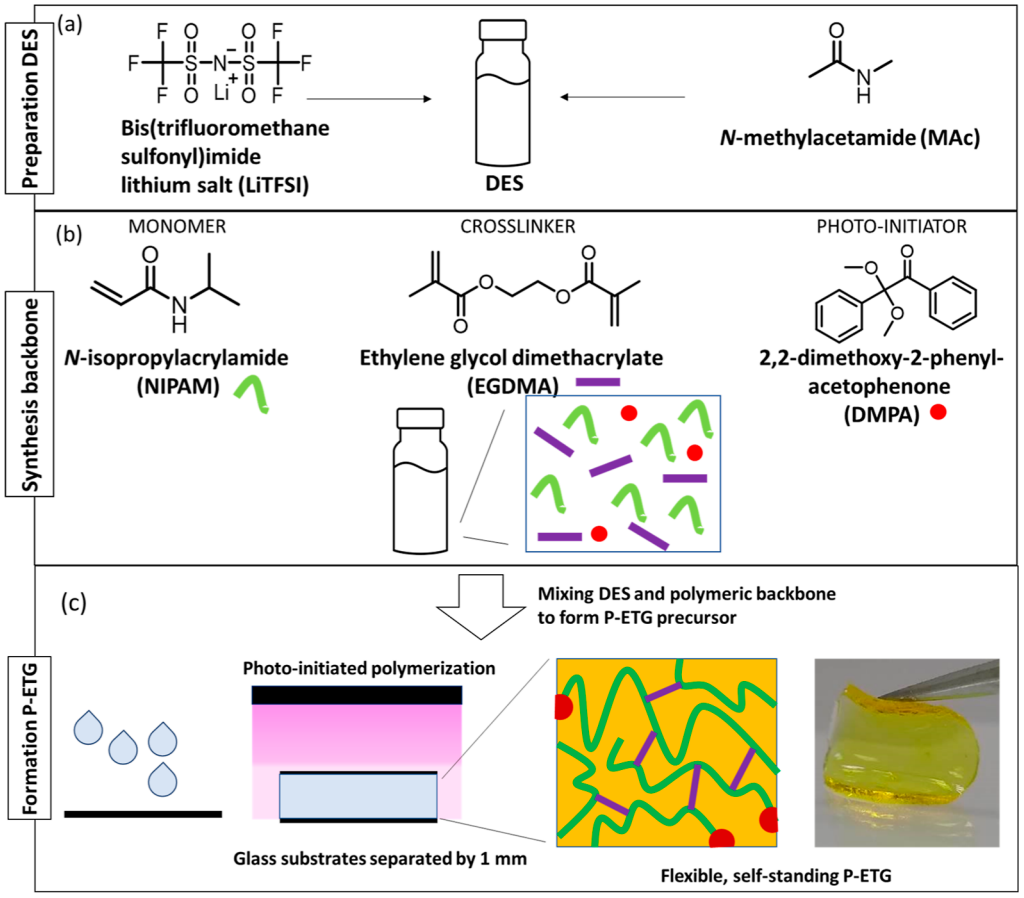

Figure 1. Overview of the synthesis procedure of a P-ETG with an NIPAM-based polymeric backbone. First, (a) the DES and (b) the polymeric matrix precursors are prepared by stirring the components. Second, (c) the P-ETG precursor is prepared by mixing both the DES and the polymeric matrix precursor and transferred to a glass mold to be UV cured, resulting in a flexible, self-standing electrolyte. The volume ratio of the DES to polymer precursor was varied from 85:15, 70:30, and 55:45. The molar ratio of the DMPA initiator to monomer and cross-linker in the polymer precursor was fixed at 5:100, while the molar ratio of EGDMA/NIPAM was 10:90.

metric analysis (TGA, Q500 TA Instruments, High-T Pt sample pan) was performed from room temperature to 600 °C (20 °C min^{-1}, continuous nitrogen flow of 90 mL min^{-1}). For DES and P-ETG, the TGA chamber was flushed for 20 min before starting the measurement. This flushing step was not applied for the liquid electrolyte, as a mass loss of around 30% was already measured during flushing. The mechanical properties of the NIPAM-based P-ETGs were studied by using dynamic mechanical analysis (DMA). A TA Instruments DMA Q800 V21.3 Build 96 instrument was used in compression mode. Stress−strain curves were obtained by a static mechanical test with a 0.05 N preload force and a rate of 1.0 N/min. The P-ETGs were cut into a cylindrical shape with a height of approximately 1 mm and a diameter of 10 mm. The exact sample geometry was measured and used for the evaluation of each individual measurement. The tests were carried out at 25 °C at least three times for each sample. The modulus was calculated from the slope of the linear section of the stress−strain curve from 8.9 to 9.1%.

Electrochemical Characterization. The ionic conductivity of the P-ETG electrolyte was measured in a broad temperature range (−10 to 60 °C, BINDER furnace KB53 E3.1) by EIS in a symmetric stainless steel|P-ETG|stainless steel Swagelok-type cell. EIS (Bio-Logic, SP-300) was performed by perturbing the open-circuit potential (OCP) with an AC sinusoidal potential of 10 mV amplitude over a frequency range of 10 kHz−100 mHz. Multiple P-ETG samples of identical compositions were measured. Linear sweep voltammetry (LSV) and cyclic voltammetry (CV) tests (Bio-Logic, SP-300) were performed to investigate the electrochemical stability and lithium stripping/plating capability of the P-ETG electrolyte at room temperature. The P-ETGs were placed in a coin cell between Ni foil (working electrode, 0.01 mm thickness, 12 mm diameter) and lithium metal foil (reference/counter electrode), and CV was performed between the OCP and −1 V vs Li^+/Li (1 mV s^{-1} − 50 mV s^{-1}). The long-term stability between the P-ETG electrolyte and Li metal was evaluated by means of a stripping−plating test in a symmetric Li|P-ETG|Li cell. A current of 0.05 mA cm^{-2} was applied for 30 min until polarity was reversed over a period of 90 h in total while monitoring the potential over the cell. The measurements were performed on a Bio-Logic SP-300 potentiostat.

Preparation of the Li|P-ETG|NMC Cells and Galvanostatic Cycling. Positive electrodes ($LiNi_{0.6}Mn_{0.2}Co_{0.2}O_2$, NMC622, Umicore) were formulated with 80 wt % $LiNi_{0.6}Mn_{0.2}Co_{0.2}O_2$ (Umicore, 0.8 g for 1 g slurry), 10 wt % carbon black (Super C65, C-NERGY, 0.1 g for 1 g slurry), and 10 wt % poly(vinylidene fluoride) (PVDF, Alfa Aesar) by mixing them in *N*-methyl-2-pyrrolidone (NMP, Alfa Aesar, >99.0%+, 1.67 g of 6 wt % PVDF in NMP for 1 g slurry), using a planetary Thinky mixer at 2000 rpm, 30 kPa, for 10 min. Next, the well-mixed slurry was tape-casted on 20 μm thick

https://doi.org/10.1021/acsomega.3c03081
ACS Omega 2023, 8, 36753−36763

aluminum foil and dried in air at 110 °C for 1 h to obtain electrodes with a thickness of approximately ∼18.7 μm (excluding current collector) and an active material loading of 0.622 mg cm^{-2} (0.109 mA h cm^{-2}, assuming a theoretical capacity of 175 mA h g^{-1} for the NMC622). For use in coin cells, a P-ETG electrolyte of appropriate size was cut by means of a hollow punch with a diameter of 14 mm. LIBs, Li|P-ETG|NMC622 (CR2025), were assembled by combining a separate positive electrode punch (10 mm diameter, ∼ 19 μm thickness excluding current collector), a separate P-ETG electrolyte monolith (14 mm diameter, 1 mm thickness), and a metal lithium punch (14 mm diameter, 0.38 mm thickness) in an argon-filled glovebox. All coin cells underwent a 16 h OCP period at room temperature prior to galvanostatic cycling between 3.0 and 4.3 V vs Li^+/Li. The electrodes were activated by two galvanostatic charge/discharge cycles (termed formation cycles) at C/20 between 3.0 and 4.3 V vs Li^+/Li in the constant-current (CC) mode. Long-term galvanostatic cycling tests were conducted at three C-rates, i.e., C/5, C/2, and 1C, at room temperature in the CC mode. The rate performance was evaluated by measuring the sensitivity of the discharge capacity to the C-rate (C/10 to 5C) at room temperature in the CC mode.

RESULTS AND DISCUSSION

P-ETGs incorporate a DES (consisting of LiTFSI and MAc in a 1:4 molar ratio; Figure 1a) within a polymeric backbone. In this work, the latter is formed by UV curing of a mixture of NIPAM monomer, a cross-linker (EGDMA), a photoinitiator (DMPA) (Figure 1b), and DES. NIPAM exhibits good miscibility with the DES, avoiding phase separation during further treatment. The P-ETG showed the most favorable mechanical characteristics (e.g., flexibility and toughness) when the (monomer/cross-linker)/initiator molar ratios in the precursor solution were fixed at (90:10):5 using the NIPAM backbone. Therefore, this ratio was chosen to develop the P-ETG with the NIPAM backbone. The volume content of the DES in the P-ETG precursor was varied between 55 and 90 vol %, i.e., 55, 70, 85, and 90 vol %. Although the former three had high structural integrity (Figure 1c), increasing the DES content up to 90 vol % resulted in a P-ETG with a soft, viscous consistency, which could not easily be handled. The ATR-FT-IR spectra, together with the assigned vibrations of the P-ETGs with different DES loadings, are given in Figure S1 and Table S1.

Three P-ETG electrolyte compositions were prepared, each with a different DES concentration. The exact composition, along with an overview of their anodic stability limit, conductivity at 25 °C, and elastic modulus, is summarized in Table 1.

Properties of the P-ETG Electrolyte. The ionic conductivity of the P-ETGs was determined by means of EIS between −10 and 60 °C (Table 2 and Figure 2). The ionic conductivity of the P-ETGs strongly correlates with the volumetric content of the enclosed DES (Table 2) and reaches 0.82 mS cm^{-1} for the P-ETG-85 at 25 °C. In Figure 2, the Arrhenius plot can be described with the Vogel−Tammann−Fulcher (VTF) equation

$$\sigma = \sigma_0 e^{\frac{-B}{(T-T_0)}} \quad (1)$$

In eq 1, the pre-exponential factor σ_0 (the conductivity at infinite temperature) is a function of the effective number of charge carriers in the electrolyte and therefore is correlated to the DES content of the P-ETG. The pseudoactivation energy B is inversely proportional to the DES content.[42,43]

Table 1. Sample Name, Volume Ratio of DES (Selected Samples P-ETG-x Were Prepared with a Specific DES Volume Content, x-Value from 55 to 85 vol %), Anodic Stability Limit, Ionic Conductivity at 25 °C, and Elastic Modulus of the Electrolytes Presented in This Article

name	vol % DES	anodic stability limit vs Li^+/Li (V)	ionic conductivity at 25 °C (mS cm^{-1})	elastic modulus (MPa)
P-ETG-55	55	≈3.55	$1.8 \pm 0.5 \times 10^{-3}$	4.9 ± 0.3
P-ETG-70	70	≈4.60	$7.0 \pm 0.9 \times 10^{-2}$	$5.1 \pm 0.1 \times 10^{-1}$
P-ETG-85	85	≈5.00	$8.2 \pm 0.2 \times 10^{-1}$	$4.7 \pm 0.2 \times 10^{-2}$

Techniques like LSV or CV, which involve increasing the potential while monitoring the current, are frequently used to determine an electrolyte's potential limit. This limit, indicated by a significant increase in current, is related to electrolyte degradation at the working interface. The electrochemical stability window of the set of P-ETGs was determined by LSV. In the cathodic scan (Figure S2), the process occurs around 1.2−1.4 V vs Li^+/Li corresponding to the reduction of $TFSI^-$,[44] whereas the process around 0.3−0.5 V vs Li^+/Li can be tentatively assigned to the reduction of amides in the P-ETGs (both MAc and polymer backbone).[45] In the anodic scan (Figure 3), the oxidation process occurred around 4.6−4.8 V vs Li^+/Li for P-ETG-85, which may originate from the oxidation of the $TFSI^-$ anions.[40] Although this procedure seems simple, it might be difficult to understand the LSV data fully. With this approach, it can be challenging to determine if a current rise is substantial enough to be caused by the electrolyte's electrochemical degradation, especially when the electrolyte's mass transport, thickness, conductivity, and the used scan rate all affect the observed current. The P-ETG-85 electrolytes exhibit a higher current in the LSV studies than the P-ETG-55 electrolytes due to the difference in ionic conductivities (Figure S3). The issues highlight the limits of the commonly used current cutoff approach as it makes the decision of the oxidative stability limit and the comparison between samples more difficult. Another method to determine the electrolyte's electrochemical stability limit is using the current's derivative to more precisely detect changes in the LSV, as the derivative graphs show a modest peak before the final increase in current.[46] The onset of those peaks appears at around 4.9 and 4.6 V vs Li^+/Li for P-ETG-85, and P-ETG-70, respectively (Figure S4). Again, the determination of these values will largely depend on the y-axis scale. Li et al.[47] suggested an alternative approach to the traditional CV experiment, which places a strong emphasis on the reaction's reversibility. The potential limit is gradually raised from the OCV to higher potentials with each cycle. The arbitrary point where the Faradaic capacity equaled 1% of the cathodic capacity was chosen as the oxidation limit. Hernández et al.[48] evaluated several electrochemical methods, including staircase voltammetry (SV), synthetic charge−discharge profile voltammetry (SCPV), and cutoff increase cell cycling, that may be used to examine the electrochemical stability of polymer electrolytes. Nonetheless, they show that there is not a single, reliable method or process for determining the electrochemical stability window of polymer electrolytes. In this work, both

https://doi.org/10.1021/acsomega.3c03081
ACS Omega 2023, 8, 36753−36763

Table 2. Ionic Conductivity, Together with VTF Model Parameters for P-ETG-85, P-ETG-70, and P-ETG-55 Electrolytes[a]

	ionic conductivity (mS cm^{-1})			VTF parameters		
	25 °C	40 °C	55 °C	σ_0 (mS cm^{-1})	B (K)	T_0 (K)
P-ETG-55	$1.8 \pm 0.5 \times 10^{-3}$	$7.8 \pm 0.3 \times 10^{-3}$	$2.0 \pm 0.5 \times 10^{-2}$	219	1216	194
P-ETG-70	$7.0 \pm 0.9 \times 10^{-2}$	$1.8 \pm 0.4 \times 10^{-1}$	$3.8 \pm 0.9 \times 10^{-1}$	381	1029	179
P-ETG-85	$8.2 \pm 0.2 \times 10^{-1}$	$1.6 \pm 0.4\ 10^{0}$	$2.9 \pm 0.6\ 10^{0}$	467	767	178
DES	1.4	3.2	6.7			

[a]The ionic conductivity of the DES is given as a reference.

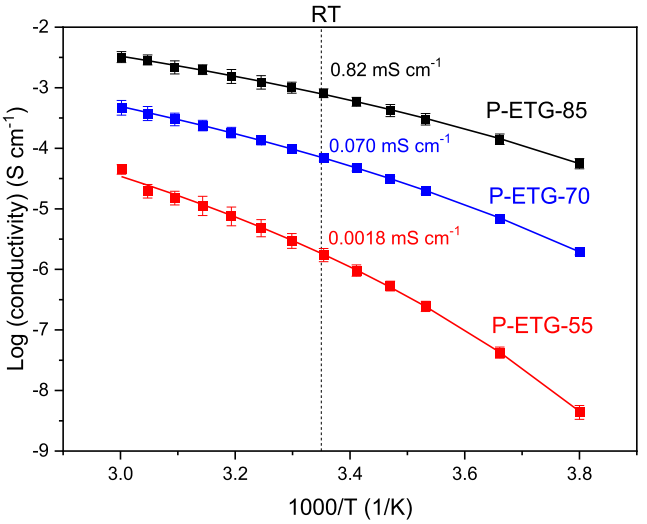

Figure 2. Ionic conductivity of P-ETG-85, P-ETG-70, and P-ETG-55 as a function of temperature. The plotted values for each electrolyte composition are averages resulting from three separate measurements. The standard deviation is represented as error bars around the measuring points. The VTF model is fitted for each composition (full line); error bars are based on the standard error of the mean.

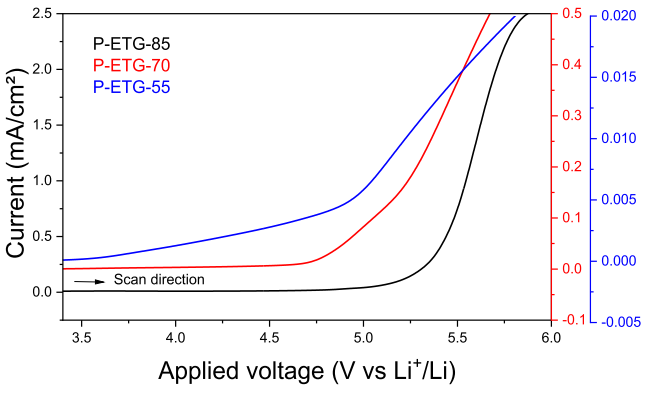

Figure 3. Anodic LSV of NIPAM-based P-ETG-85, P-ETG-70, and P-ETG-55 at a scan rate of 10 mV s^{-1}. Working electrode and counter/reference electrode are stainless steel and lithium metal, respectively.

LSV (Figure 3) and SV (Figure S5) were performed to measure the anodic stability of our three P-ETG electrolytes. Although we are aware of the limitations of each technique, they give an indication of the trend in anodic stability among our three P-ETG electrolytes (Table 3).

With increasing DES content, the P-ETGs' anodic stability limit is extended to higher potentials, which may be caused by the interaction between the DES components and the polymeric backbone. De Sloovere et al.[49] observed an increase in anodic stability with increasing NaTFSI concentration in a DES consisting of NaTFSI and MAc. The increasing concentration caused the replacement of the MAc−MAc hydrogen bonds with strong ionic interactions between MAc, Na^+, and $TFSI^-$. This lowered MAc's HOMO energy level compared to $TFSI^-$, leading to increased anodic stability.[49] The anodic stability of the DES used in this work, a lithium-based counterpart, may also be improved by such ionic interactions. When the DES is incorporated into a polymer matrix, this may influence these ionic interactions. In our electrolyte, the amide groups in the polymeric backbone may also coordinate Li^+ and $TFSI^-$ ions, effectively decreasing the extent of ionic interactions with MAc and decreasing the anodic stability. With increasing polymer content (i.e., decreasing DES content), MAc will form fewer ionic interactions, meaning that the P-ETGs' anodic stability will be lower. Raman spectra of MAc, DES, and the P-ETGs with different DES loadings are presented in Figure S6 and Table S2.[50,51] The Raman spectra of the different P-ETG compositions correspond to the spectra of DES, which is also the main component of the P-ETG. The absence of additional peaks or large peak shifts could mean that the same chemical interactions/bonds are largely preserved.

Poor mechanical performance, resulting in the loss of contact between the electrolyte and electrodes, hampers the application of solid-state electrolytes in energy storage devices. As such, solid electrolytes should be robust to prevent Li dendrite growth, and elastic to allow an intimate contact with the electrodes.[52] By combining the beneficial characteristics of solid and liquid electrolytes, our P-ETG hybrid solid-state electrolyte systems provide sufficient ionic conductivity, good mechanical strength, and improved flexibility. To study the mechanical properties of the P-ETGs, DMA was performed, and the compressive stress−strain curves are shown in Figure S7. P-ETG-85, the most flexible electrolyte, showed plastic deformation after the compressive test in the form of cracks and tears. P-ETG-70 and P-ETG-55 did not show plastic deformation. The elastic moduli, measured at the linear elastic part of the stress−strain curve, are 0.047 ± 0.002 0.51 ± 0.01,

Table 3. Experimental Conditions for LSV and SV Measurements and the Anodic Stability Limits of P-ETG-85, P-ETG-70, and P-ETG-55

technique	working electrode	potential range V vs Li^+/Li	scan rate	P-ETG-85 (V)	P-ETG-70 (V)	P-ETG-55 (V)
LSV	stainless steel	3−6	10 mV s^{-1}	5.0	4.6	3.6
SV	stainless steel	3−6	100 mV step h^{-1}	4.5	4.4	4.1

https://doi.org/10.1021/acsomega.3c03081
ACS Omega 2023, 8, 36753−36763

and 4.9 ± 0.3 MPa for P-ETG-85, P-ETG-70, and P-ETG-55, respectively. This corroborates the visual observation of increasing stiffness and elasticity with decreasing DES content. For comparison, Khurana et al. reported a cross-linked polyethylene-poly(ethylene oxide) solid polymer electrolyte with excellent resistance to dendrite growth, and a modulus of about 0.1 MPa at 90 °C.[53]

The ionic conductivity, anodic stability, and compressive stress−strain measurements indicate that P-ETG-85 is the most promising hybrid solid electrolyte for application in batteries with high-potential positive electrode materials. Therefore, the remainder of this work is solely focused on the P-ETG-85 composition.

The thermal degradation of P-ETG-85 was determined by means of TGA under an inert atmosphere. The DES and a conventional electrolyte [1 M $LiPF_6$ in EC/EMC (3/7) + 2% VC] were analyzed as references (see Figure 4). Increasing the

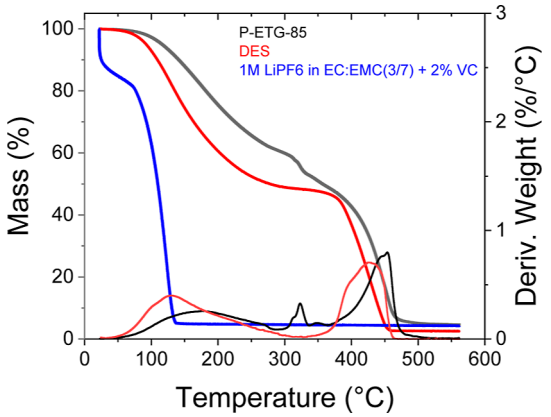

Figure 4. Thermograms of P-ETG-85, DES, and a conventional electrolyte under a nitrogen atmosphere.

temperature causes continuous evaporation of the conventional electrolyte solvent until almost all mass is lost at about 140 °C. The DES displays a gradual two-step degradation between room temperature and 460 °C, originating from the MAc and LiTFSI components. The coordination of the Li^+ ions with the MAc carbonyl moieties inhibits evaporation of the MAc.[30] This coordination postpones the loss onset and broadens the thermal stability window of the MAc in the DES. The weight loss of the P-ETGs is lower than that of the pure DES as the most volatile compound, the MAc, is present in a lower concentration and is encapsulated in the polymeric backbone structure. This indicates an increased safety of the P-ETG electrolyte compared to conventional electrolytes thanks to the nonflammability of the DES.

(Electro)chemical Compatibility. When applying a DES composed of choline chloride and ethylene glycol (ChCl/EG) for LIB cathode recycling, cobalt leaching efficiencies of >90% are observed.[54] Hence, it can be expected that such cation leaching also could occur when the P-ETG is in contact with NMC622, which could lead to capacity fading. To investigate the chemical compatibility between the NMC622 and DES, 610 mg of NMC622 powder was dispersed in 1.4 mL of DES, and the mixture was stirred at room temperature for 28 days under an inert atmosphere. After filtration, ICP-AES was performed on the DES to measure any transition metal (Ni, Co, and Mn) ion leaching of the NMC622. Table 4 gives the measured transition metal ion concentration (in parts per million) in the DES, together with the transition metal ion concentration detected after repeating the experiment using a conventional electrolyte (1 M $LiPF_6$ in EC/EMC (3/7) + 2% VC). Only a limited amount of Ni in ppm levels leaches out into the DES after contact with NMC622 active material. This provides a first indication that the DES is chemically compatible with the NMC622 active positive electrode material. Only small amounts (ppm-level) of Mn and Co were detected in the DES after contact with NMC622.

To detect changes in the bulk crystal structure of NMC622 after contact with DES, which would be an indication of chemical reaction and incompatibility, PXRD was carried out. The compatibility was evaluated by disassembling a coin cell after cycling (3.0−4.3 V vs Li^+/Li for 50 cycles at C/10) and studying the (electro)chemical stability between the positive electrode and solid electrolyte. It was found that there are no additional diffraction peaks in the diffractogram of the NMC622 active material powder (Figure 5, left), which indicates that within the detection limits of PXRD, the bulk layered structure is maintained after cycling. However, galvanostatic cycling may cause an increase in lithium and transition metal ion disorder, as is indicated by the decreased intensity ratio of the (003)/(104) diffraction peaks, which is a known phenomenon for NMC positive electrode materials, affecting the electrochemical properties.[55] Since the ionic radius of octahedrally coordinated Li^+ (0.76 Å) is close to that of Ni^{2+} (0.69 Å), Li^+/Ni^{2+} antisite disorder is most likely to occur. This could block the lithium diffusion pathways, causing severe capacity fade.[55,56]

To investigate the possible degradation of the P-ETG in contact with high-voltage positive electrodes, post-mortem FT-IR spectroscopy was performed, which is commonly used in this context in the literature.[46,57] Figure 5 (right) shows the ATR-FT-IR spectra of the DES, the polymeric matrix, and P-ETG-85 before and after cycling for 50 cycles. The ATR-FT-IR spectra of the P-ETG are dominated by vibrations ascribed to DES, which is due to its large volumetric proportion in the P-ETG combined with the overlapping of amide signals from MAc and the polymeric backbone. The most important vibrations are given in Table S1.[51,58−60] After cycling, the spectrum does not show any differences compared to the pristine P-ETG, suggesting that within the detection limits, no

Table 4. Concentration (in ppm) of Transition-Metal Ions (Ni, Mn, and Co) Measured in the DES or Conventional Electrolyte and Percentage of Ni, Mn, and Co from NMC622 Leached Out in the DES or Conventional Electrolyte after Mixing NMC622 Active Material in the Solvent for 28 Days

		Ni	Mn	Co
DES	concentration	6.65 ± 0.03 ppm	<5 ppb	<5 ppb
	percentage	2.4×10^{-3}%		
1 M $LiPF_6$ in EC/EMC (3/7) + 2% VC	concentration	0.140 ± 0.006 ppm	0.543 ± 0.001 ppm	0.053 ± 0.003 ppm
	percentage	3.1×10^{-4}%	3.8×10^{-3}%	3.5×10^{-4}%

https://doi.org/10.1021/acsomega.3c03081
ACS Omega 2023, 8, 36753−36763

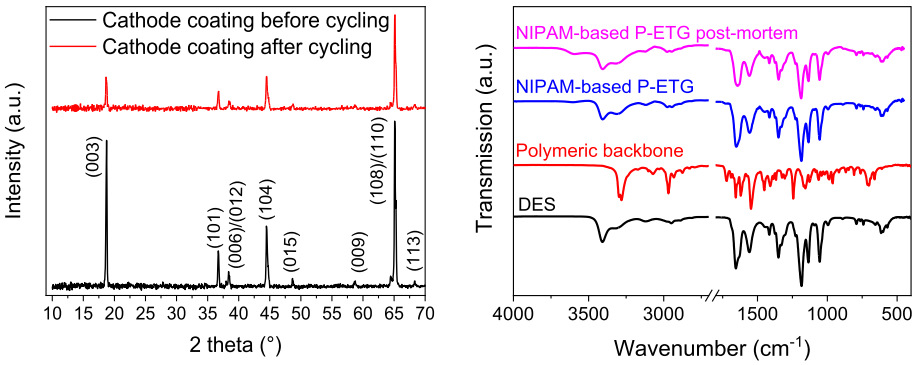

Figure 5. PXRD of NMC622 coatings before and after cycling in a coin cell with P-ETG-85 and Li metal (left) and ATR-FT-IR spectra of the P-ETG-85 before and after cycling in a coin cell with the NMC622 cathode and Li metal anode. The DES and polymeric backbone spectra are given as reference (right).

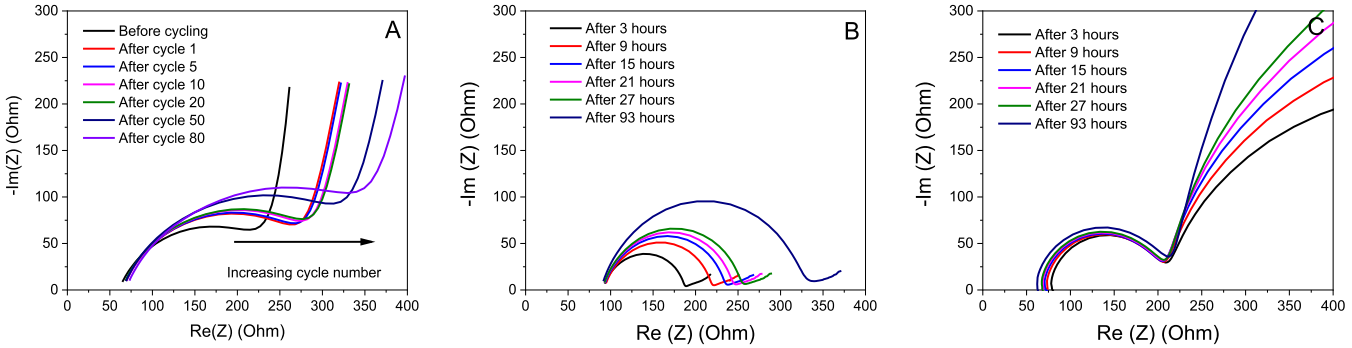

Figure 6. (a) EIS characterization of Li|P-ETG|NMC622 cells (continuous cycling at C/2), (b) EIS characterization of Li|P-ETG-85|Li symmetric cells (impedance after every 6 h of rest), and (c) EIS characterization of NMC622|P-ETG|NMC622 symmetric cells (impedance after every 6 h of rest). The NMC622 electrodes are fully charged during the symmetrical cell assembly.

decomposition products were formed by electrochemical cycling of P-ETG with high-voltage positive electrode materials. Although we like to note that FT-IR is not spatially resolved, the obtained information is averaged over the P-ETG electrolyte. Possibly, minute degradation that occurs at the interface between the electrode and electrolyte cannot be detected, despite the surface sensitivity of this technique.

NMC622|P-ETG|Li cells were continuously cycled at C/2, with EIS performed after every cycle. The EIS results (Figure 6a) show that the charge transfer resistance (R_{ct}) increases with an increasing number of cycles. This indicates that the surface films gradually become more resistant to the flow of charge with prolonged cycling. The nature of these films was further studied by EIS of symmetric cells, Li|P-ETG-85|Li (Figure 6b) as well as NMC622|P-ETG-85|NMC622 with fully charged NMC622 containing highly oxidative Ni^{4+} (Figure 6c). In the former, R_{ct} increases with time, indicating that the chemical instability of the P-ETG-85|Li interface leads to the formation of resistant films between the P-ETG electrolyte and Li metal. The long-term stability of the P-ETG electrolyte in combination with Li metal was evaluated by means of a stripping/plating test in a symmetrical Li|P-ETG-85|Li cell. The result in Figure S8 shows a constant but slow increase of polarization across the cell upon continued cycling. This indicates that a resistance interfacial layer is built up between the P-ETG and Li metal. This increase in resistance during the initial cycles suggests that when the electrolyte is reduced at the surface of the lithium metal, a solid electrolyte interface (SEI) layer is formed. The fact that the polarization still increases over time suggests that the SEI is not stable and that the reduction of the electrolyte continues over time. This is in line with the data from the time-dependent EIS measurements on Li|P-ETG-85|Li cells. Possible strategies for mitigation include improving the stability of this interface by the use of specific Li-alloys or prepassivation of the lithium metal surface.[61] In the NMC622|P-ETG-85|NMC622 cells, however, there is no significant increase in the R_{ct}, implying that the NMC622|P-ETG-85 interface is chemically stable. The resistance values (as a function of the cycle number) are presented in Figures S9 and S10, respectively.

The reactivity of P-ETG-85 with lithium metal was further investigated by CV on Ni|Li cells, where the P-ETG is sandwiched between Ni foil serving as the working electrode and Li foil serving as the reference/counter electrode (Figure S11). Lithium plating occurs on the Ni foil as its potential is swept below 0 V vs Li^+/Li. A lithium stripping peak can be observed between 0 and 1 V versus Li^+/Li in the subsequent anodic scan, indicating that the lithium plating/stripping process is partially reversible. The reversibility of this process was quantified by comparing the charge associated with the cathodic and anodic regimes of each cycle. In the first cycle, the anodic charge amounts to 33% of the cathodic charge. This value steadily increases to 42, 43, 44, and 48% for the subsequent cycles. This indicates that throughout the CV process, less than half of the plated lithium can be stripped again. In turn, this implies that the majority of the plated lithium is degraded by its reaction with the P-ETG. This results in a buildup of degradation products on the Ni|P-ETG interface, which can hinder further lithium plating. This in turn

https://doi.org/10.1021/acsomega.3c03081
ACS Omega 2023, 8, 36753−36763

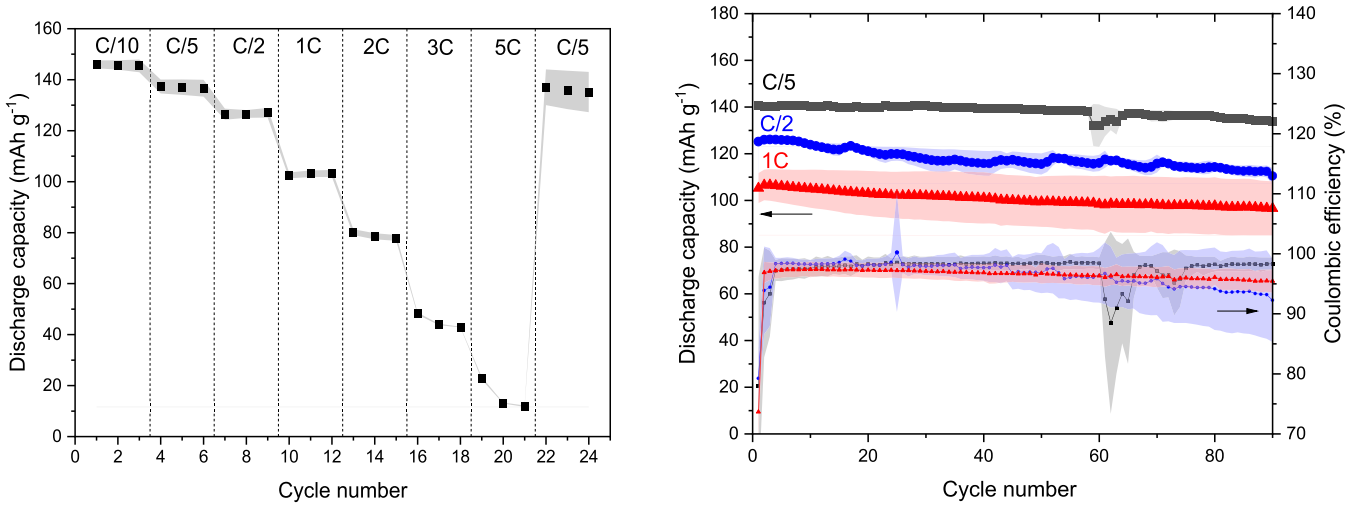

Figure 7. Impact of the C-rate on the discharge capacity (constant current−constant voltage) of the Li|P-ETG-85|NMC622 cells assembled with P-ETG-85 within the voltage window of 3.0−4.3 V vs Li^+/Li (left). Cycling stability and Coulombic efficiency of Li|P-ETG-85|NMC622 cells as a function of cycle number at 25 °C and various C-rates within the voltage window of 3.0−4.3 V vs Li^+/Li (right). The discharge capacities are the mean of three cells for each C-rate. The standard deviation is represented as filled areas around the measuring points. The capacities are normalized to the mass of the active material in the positive electrode.

explains the decreasing currents observed in subsequent CV cycles.

Battery Performance. The averaged results of the rate capability and cycle stability tests are presented in Figure 7. The cells performed well at lower C-rates, with average discharge capacities of about 146, 137, and 127 mA h g^{-1} for cycling rates of C/10, C/5, and C/2, respectively. Increasing the C-rate to 2C, 3C, and 5C lowers the reversible discharge capacity to about 79, 44, and 16 mA h g^{-1}, respectively. The lower capacities at higher discharge rates can be ascribed to the lower conductivity of the P-ETG (0.82 mS cm^{-1} for P-ETG vs 8−10 mS cm^{-1} for liquid electrolytes). The final cycles at C/5 have a discharge capacity of around 145 mA h g^{-1}, similar to the initial cycles, which implies that the low capacity at higher C-rates can be mainly attributed to the kinetics of ion transport and not due to the structural degradation of NMC622 or our P-ETG-85 electrolyte. The latter agrees with our anodic stability tests presented in Figure 3. The electrochemical performance of the NIPAM-based P-ETG-85 in conjunction with NMC622 is remarkably higher than that of the previously reported P-ETG with the ACMO backbone (Figure S12).

In the cycling stability test, 95.2, 88.3, and 87.7% of the initial capacity remained after 90 cycles at C/5, C/2, and 1C, respectively. The Coulombic efficiencies are above 95% for C/5, C/2, and 1C. Loss of capacity is observed after multiple cycles, which may be related to the growth of resistant surface films with prolonged cycling times. As a reference, the discharge capacity vs cycle number of cells with a liquid electrolyte are also presented in Figures S13 and S14. The capacity retention after 90 cycles of cells with liquid electrolytes is higher compared to that of the cells with the P-ETG electrolyte. This could be explained by the lower ionic conductivity and buildup of a resistant interphase between the electrode and electrolyte. The capacity−voltage plots for the (dis)charge of a single cell using NIPAM-based P-ETG-85 at the 50th cycle cycled at C/5, C/2, and 1C C-rates are shown in Figure S15. The evolution of discharge capacity for a NMC622|NIPAM-based P-ETG-85|Li cell at a C-rate of 1C over 240 cycles is presented in Figure S16.

Despite the low positive electrode's areal capacity, obtaining scientific insights into the compatibility of the electrolytes with commercially relevant positive electrode materials, such as NMC622, is important. Therefore, the main goal of the work presented here is solely to introduce and demonstrate the compatibility between our promising P-ETG electrolyte and the Ni-rich NMC positive electrode material NMC622. As a reference, Figure S17 gives the discharge capacity of a full cell with a positive electrode with a higher loading (0.98 mA h cm^{-2}), resulting in a lower discharge capacity and capacity fading. This could be explained by the fact that the thicker positive electrodes have a longer ionic pathway, increasing the resistance, especially as the P-ETG electrolyte is not able to fill all the pores inside the electrode. The next goal could be improving ion and charge transport between the P-ETG electrolyte and electrode by impregnating the P-ETG electrolyte in the pores of the positive electrode.

CONCLUSIONS

In this work, we demonstrate a promising, flexible P-ETG electrolyte for LIBs, composed of a DES enclosed within an NIPAM-based polymeric backbone. This P-ETG is compatible with high-potential positive electrode materials for LIBs, as it shows a broad electrochemical stability window (1.5−5.0 V vs Li^+/Li) and a high ionic conductivity at room temperature (0.82 mS cm^{-1}). The P-ETG also displays higher thermal stability compared to conventional liquid electrolytes [i.e., 1 M $LiPF_6$ in EC/EMC (3/7) + 2% VC], leading to a suppressed flammability, which results in increased safety in the use of battery applications, such as electric vehicles. PXRD, ATR-FT-IR, ICP-AES, and EIS indicated that the P-ETG electrolyte and NMC622 active positive electrode material are chemically compatible. However, a chemical instability of the P-ETG-85/Li interface leads to the formation of resistant films. The Li|NMC622 coin cells assembled with this NIPAM-based P-ETG as the electrolyte were found to deliver a capacity of 134, 110, and 97 mA h g^{-1} over 90 cycles at C/5, C/2, and 1C. The Coulombic efficiency is exceeding 95% for C/5, C/2, and 1C. In contrast to the former generation of P-ETG, which had the

https://doi.org/10.1021/acsomega.3c03081
ACS Omega 2023, 8, 36753−36763

limitation that it could only function in conjunction with $LiFePO_4$, a low energy density cathode material, our novel composition of P-ETG, overcomes this limitation and elevates the P-ETG up to the league of the real-world high-voltage batteries built with high Ni-NMC, such as NMC622. Therefore, it is concluded that the NIPAM-based P-ETG holds potential as an inexpensive and flexible electrolyte for the next-generation solid-state Li-ion batteries with high-potential positive electrode materials.

■ ASSOCIATED CONTENT

Supporting Information

The Supporting Information is available free of charge at https://pubs.acs.org/doi/10.1021/acsomega.3c03081.

ATR-FT-IR spectra of the selected P-ETG samples with different DES loadings; assignment of the main vibrations (cm^{-1}) in the FT-IR spectra for the DES and polymeric backbone reference; cathodic LSV of the NIPAM-based P-ETG-85; anodic LSV of the NIPAM-based P-ETG-85 and P-ETG-70; derivative with respect to potential for P-ETG-85, P-ETG-70, and P-ETG-55; current response of P-ETG-85, P-ETG-70, and P-ETG-55 at different potential steps; Raman spectra of MAc, DES, and selected P-ETG samples with different DES loadings; assignment of the main vibrations (cm^{-1}) in the Raman spectra for the DES; stress−strain curves for P-ETG-85, P-ETG-70, and P-ETG-55 in compression mode; stripping/plating of the NIPAM-based P-ETG-85 electrolyte in a symmetrical Li|P-ETG | Li cell; electrolyte (R_s) and charge transfer resistance (R_{ct}), as a function of cycle number, extracted from fitting the Nyquist plot from a Li|P-ETG-85|NMC622 cell; electrolyte (R_s) and charge transfer resistance (R_{ct}), as a function of resting time (in hours) of the symmetric cells Li|NIPAM-based P-ETG|Li and NMC622|NIPAM-based P-ETG-85|NMC622; cyclic voltammograms of the NIPAM-based P-ETG-85 electrolyte; capacity−voltage plots for the charge and discharge of a single NMC622|Li cell with the ACMO-based P-ETG-85; impact of C-rate on the discharge capacity (constant current−constant voltage) of the Li|conventional electrolyte|NMC622 cells; cycling stability and Coulombic efficiency of Li|conventional electrolyte|NMC622 cells as a function of cycle number; capacity−voltage plots for the (dis)charge of a single cell using NIPAM-based P-ETG-85 at the 50th cycle cycled at C/5, C/2, and 1C C-rates; evolution of discharge capacity for a NMC622|NIPAM-based P-ETG-85|Li cell at a C-rate of 1C over 240 cycles; and cycling stability of LTO|NMC622 cells as a function of cycle number at 25 °C (PDF)

■ AUTHOR INFORMATION

Corresponding Authors

An-Sofie Kelchtermans − *Institute for Materials Research (imo-imomec), Materials Chemistry, DESINe Group, Hasselt University, Diepenbeek 3590, Belgium; EnergyVille, Genk 3600, Belgium;* orcid.org/0000-0001-6957-2216; Email: ansofie.kelchtermans@uhasselt.be

An Hardy − *Institute for Materials Research (imo-imomec), Materials Chemistry, DESINe Group, Hasselt University, Diepenbeek 3590, Belgium; IMEC vzw, Division Imomec Associated Laboratory, Diepenbeek 3590, Belgium; EnergyVille, Genk 3600, Belgium;* orcid.org/0000-0002-5012-0356; Email: an.hardy@uhasselt.be

Authors

Bjorn Joos − *Institute for Materials Research (imo-imomec), Materials Chemistry, DESINe Group, Hasselt University, Diepenbeek 3590, Belgium; IMEC vzw, Division Imomec Associated Laboratory, Diepenbeek 3590, Belgium; EnergyVille, Genk 3600, Belgium;* orcid.org/0000-0001-8697-8330

Dries De Sloovere − *Institute for Materials Research (imo-imomec), Materials Chemistry, DESINe Group, Hasselt University, Diepenbeek 3590, Belgium; IMEC vzw, Division Imomec Associated Laboratory, Diepenbeek 3590, Belgium; EnergyVille, Genk 3600, Belgium;* orcid.org/0000-0001-9358-1278

Andreas Paulus − *Institute for Materials Research (imo-imomec), Materials Chemistry, DESINe Group, Hasselt University, Diepenbeek 3590, Belgium; IMEC vzw, Division Imomec Associated Laboratory, Diepenbeek 3590, Belgium; EnergyVille, Genk 3600, Belgium;* orcid.org/0000-0002-5588-6879

Jonas Mercken − *Institute for Materials Research (imo-imomec), Materials Chemistry, DESINe Group, Hasselt University, Diepenbeek 3590, Belgium; IMEC vzw, Division Imomec Associated Laboratory, Diepenbeek 3590, Belgium; EnergyVille, Genk 3600, Belgium*

Satish Kumar Mylavarapu − *Institute for Materials Research (imo-imomec), Materials Chemistry, DESINe Group, Hasselt University, Diepenbeek 3590, Belgium; IMEC vzw, Division Imomec Associated Laboratory, Diepenbeek 3590, Belgium; EnergyVille, Genk 3600, Belgium;* orcid.org/0000-0002-5386-8503

Ken Elen − *Institute for Materials Research (imo-imomec), Materials Chemistry, DESINe Group, Hasselt University, Diepenbeek 3590, Belgium; IMEC vzw, Division Imomec Associated Laboratory, Diepenbeek 3590, Belgium; EnergyVille, Genk 3600, Belgium;* orcid.org/0000-0001-6907-0355

Wouter Marchal − *Institute for Materials Research (imo-imomec), Materials Chemistry, Analytical & Circular Chemistry (ACC), Hasselt University, Diepenbeek 3590, Belgium;* orcid.org/0000-0001-5105-8112

Alexander Tesfaye − *Umicore, Corporate Research & Development, Olen 2230, Belgium*

Travis Thompson − *Umicore, Corporate Research & Development, Olen 2230, Belgium*

Marlies K. Van Bael − *Institute for Materials Research (imo-imomec), Materials Chemistry, DESINe Group, Hasselt University, Diepenbeek 3590, Belgium; IMEC vzw, Division Imomec Associated Laboratory, Diepenbeek 3590, Belgium; EnergyVille, Genk 3600, Belgium;* orcid.org/0000-0002-5516-7962

Complete contact information is available at: https://pubs.acs.org/10.1021/acsomega.3c03081

Notes

The authors declare no competing financial interest.

■ ACKNOWLEDGMENTS

This project received financial support from VLAIO and Umicore (Baekeland project HBC.2018.2097).

REFERENCES

(1) Armand, M.; Tarascon, J. M. Building better batteries. *Nature*; Nature Publishing Group, 2008; Vol. *451*, pp 652−657, Feb. 07, no. 7179.

(2) Jeong, G.; Kim, Y. U.; Kim, H.; Kim, Y. J.; Sohn, H. J. Prospective materials and applications for Li secondary batteries. *Energy and Environmental Science*; The Royal Society of Chemistry, 2011; Vol. *4*, pp 1986−2002. Jun. 02, no. 6.

(3) Yue, L.; et al. All solid-state polymer electrolytes for high-performance lithium ion batteries. *Energy Storage Materials*; Elsevier B.V., 2016; Vol. *5*, pp 139−164. Oct. 01.

(4) Deng, D. Li-ion batteries: basics, progress, and challenges,. *Energy Sci. Eng.* **2015**, *3* (5), 385−418.

(5) Manthiram, A. An Outlook on Lithium Ion Battery Technology,. *ACS Cent. Sci.* **2017**, *3* (10), 1063−1069.

(6) Chen, R.; Zhao, T.; Zhang, X.; Li, L.; Wu, F. Advanced cathode materials for lithium-ion batteries using nanoarchitectonics. *Nanoscale Horizons*; Royal Society of Chemistry, 2016; Vol. *1*, pp 423−444. Nov. 01, no. 6.

(7) Van Mierlo, J.; Berecibar, M.; El Baghdadi, M.; De Cauwer, C.; Messagie, M.; Coosemans, T.; Jacobs, V.; Hegazy, O. Beyond the State of the Art of Electric Vehicles: A Fact-Based Paper of the Current and Prospective Electric Vehicle Technologies,. *World Electr. Veh. J.* **2021**, *12* (1), 20.

(8) Lyu, Y.; Wu, X.; Wang, K.; Feng, Z.; Cheng, T.; Liu, Y.; Wang, M.; Chen, R.; Xu, L.; Zhou, J.; et al. An Overview on the Advances of LiCoO2 Cathodes for Lithium-Ion Batteries,. *Adv. Energy Mater.* **2021**, *11* (2), 2000982.

(9) Huang, H.; Yin, S. C.; Nazar, L. F. Approaching Theoretical Capacity of LiFePO[sub 4] at Room Temperature at High Rates. *Electrochem. Solid-State Lett.* **2001**, *4* (10), 170−173.

(10) Yan, W.; Liu, Y.; Chong, S.; Zhou, Y.; Liu, J.; Zou, Z. Lithium-Rich Cathode Materials for High Energy-Density Lithium-Ion Batteries,. *Prog. Chem.* **2017**, *29* (2−3), 198−209.

(11) Kalaiselvi, K.; Kalaignan, G. P. Yttrium-substituted LiNi 0.3 Mn 0.3 Co 0.3 O 2 cathode material with enhanced cycling stability for rechargeable lithium-ion batteries,. *Ionics (Kiel).* **2019**, *25* (3), 991−997.

(12) Yaqub, A.; Lee, Y. J.; Hwang, M. J.; Pervez, S. A.; Farooq, U.; Choi, J. H.; Kim, D.; Choi, H. Y.; Cho, S. B.; Doh, C. H. Low temperature performance of graphite and LiNi0.6Co 0.2Mn0.2O2 electrodes in Li-ion batteries,. *J. Mater. Sci.* **2014**, *49* (22), 7707−7714.

(13) Xiao, Z. W.; Zhang, Y. J.; Wang, Y. F. Synthesis of high-capacity LiNi0.8Co0.1Mn0.1O2 cathode by transition metal acetates,. *Trans. Nonferrous Met. Soc. China (English Ed.* **2015**, *25* (5), 1568−1574.

(14) Noh, H. J.; Youn, S.; Yoon, C. S.; Sun, Y. K. Comparison of the structural and electrochemical properties of layered Li[NixCoyMnz]-O2 (x = 1/3, 0.5, 0.6, 0.7, 0.8 and 0.85) cathode material for lithium-ion batteries,. *J. Power Sources* **2013**, *233*, 121−130.

(15) Greenwood, M.; Wentker, M.; Leker, J. A bottom-up performance and cost assessment of lithium-ion battery pouch cells utilizing nickel-rich cathode active materials and silicon-graphite composite anodes,. *J. Power Sources Adv.* **2021**, *9*, 100055.

(16) Bak, S. M.; Hu, E.; Zhou, Y.; Yu, X.; Senanayake, S. D.; Cho, S. J.; Kim, K. B.; Chung, K. Y.; Yang, X. Q.; Nam, K. W. Structural Changes and Thermal Stability of Charged $LiNi_xMn_yCo_zO_2$ Cathode Materials Studied by Combined In Situ Time-Resolved XRD and Mass Spectroscopy. *ACS Appl. Mater. Interfaces* **2014**, *6* (24), 22594−22601.

(17) Geng, L.; Liu, J.; Wood, D. L.; Qin, Y.; Lu, W.; Jafta, C. J.; Bai, Y.; Belharouak, I. Probing Thermal Stability of Li-Ion Battery Ni-Rich Layered Oxide Cathodes by means of Operando Gas Analysis and Neutron Diffraction,. *ACS Appl. Energy Mater.* **2020**, *3* (7), 7058−7065.

(18) Yan, X.; Li, Z.; Wen, Z.; Han, W. Li/Li7La3Zr2O12/LiFePO4 all-solid-state battery with ultrathin nanoscale solid electrolyte,. *J. Phys. Chem. C* **2017**, *121* (3), 1431−1435.

(19) Mindemark, J.; Lacey, M. J.; Bowden, T.; Brandell, D. Beyond PEO—Alternative host materials for Li+-conducting solid polymer electrolytes,. *Prog. Polym. Sci.* **2018**, *81*, 114−143.

(20) Lian, P. J.; Zhao, B. S.; Zhang, L. Q.; Xu, N.; Wu, M. T.; Gao, X. P. Inorganic sulfide solid electrolytes for all-solid-state lithium secondary batteries,. *J. Mater. Chem. A* **2019**, *7* (36), 20540−20557.

(21) Stramare, S.; Thangadurai, V.; Weppner, W. Lithium Lanthanum Titanates: A Review,. *Chem. Mater.* **2003**, *15* (21), 3974−3990.

(22) Takada, K. Progress and prospective of solid-state lithium batteries,. *Acta Mater.* **2013**, *61* (3), 759−770.

(23) Teng, S.; Tan, J.; Tiwari, A. Recent developments in garnet based solid state electrolytes for thin film batteries,. *Curr. Opin. Solid State Mater. Sci.* **2014**, *18* (1), 29−38.

(24) Cao, C.; Li, Z. B.; Wang, X. L.; Zhao, X. B.; Han, W. Q. Recent advances in inorganic solid electrolytes for lithium batteries,. *Front. Energy Res.* **2014**, *2* (JUN), 1−10.

(25) Néouze, M. A.; Le Bideau, J.; Gaveau, P.; Bellayer, S.; Vioux, A. Ionogels, New Materials Arising from the Confinement of Ionic Liquids within Silica-Derived Networks,. *Chem. Mater.* **2006**, *18* (17), 3931−3936.

(26) Wang, C.; Liang, J.; Zhao, Y.; Zheng, M.; Li, X.; Sun, X. All-solid-state lithium batteries enabled by sulfide electrolytes: from fundamental research to practical engineering design,. *Energy Environ. Sci.* **2021**, *14* (5), 2577−2619.

(27) Zhou, D.; Shanmukaraj, D.; Tkacheva, A.; Armand, M.; Wang, G. Polymer Electrolytes for Lithium-Based Batteries: Advances and Prospects,. *Chem.* **2019**, *5* (9), 2326−2352.

(28) Lu, Y.; Korf, K.; Kambe, Y.; Tu, Z.; Archer, L. A. Ionic-Liquid-Nanoparticle Hybrid Electrolytes: Applications in Lithium Metal Batteries,. *Angew. Chem.* **2014**, *53*, 488.

(29) Sirisopanaporn, C.; Fernicola, A.; Scrosati, B. New, ionic liquid-based membranes for lithium battery application,. *J. Power Sources* **2009**, *186* (2), 490−495.

(30) Joos, B.; Volders, J.; da Cruz, R. R.; Baeten, E.; Safari, M.; Van Bael, M. K.; Hardy, A. T. Polymeric Backbone Eutectogels as a New Generation of Hybrid Solid-State Electrolytes,. *Chem. Mater.* **2020**, *32* (9), 3783−3793.

(31) Liu, K.; Wang, Z.; Shi, L.; Jungsuttiwong, S.; Yuan, S. Ionic liquids for high performance lithium metal batteries,. *J. Energy Chem.* **2021**, *59*, 320−333.

(32) Chatterjee, K.; Pathak, A. D.; Lakma, A.; Sharma, C. S.; Sahu, K. K.; Singh, A. K. Synthesis, characterization and application of a non-flammable dicationic ionic liquid in lithium-ion battery as electrolyte additive,. *Sci. Reports* **2020**, *10* (1), 9606.

(33) Joos, B.; Vranken, T.; Marchal, W.; Safari, M.; Van Bael, M. K.; Hardy, A. T. Eutectogels: A New Class of Solid Composite Electrolytes for Li/Li-Ion Batteries,. *Chem. Mater.* **2018**, *30* (3), 655−662.

(34) Albertus, P.; Anandan, V.; Ban, C.; Balsara, N.; Belharouak, I.; Buettner-Garrett, J.; Chen, Z.; Daniel, C.; Doeff, M.; Dudney, N. J.; et al. Challenges for and Pathways toward Li-Metal-Based All-Solid-State Batteries,. *ACS Energy Lett.* **2021**, *6* (4), 1399−1404.

(35) Tian, Y.; Shi, T.; Richards, W. D.; Li, J.; Kim, J. C.; Bo, S. H.; Ceder, G. Compatibility issues between electrodes and electrolytes in solid-state batteries,. *Energy Environ. Sci.* **2017**, *10* (5), 1150−1166.

(36) Ren, X.; Zou, L.; Jiao, S.; Mei, D.; Engelhard, M. H.; Li, Q.; Lee, H.; Niu, C.; Adams, B. D.; Wang, C.; et al. High-concentration ether electrolytes for stable high-voltage lithium metal batteries,. *ACS Energy Lett.* **2019**, *4* (4), 896−902.

(37) Jiao, S.; Ren, X.; Cao, R.; Engelhard, M. H.; Liu, Y.; Hu, D.; Mei, D.; Zheng, J.; Zhao, W.; Li, Q.; et al. Stable cycling of high-voltage lithium metal batteries in ether electrolytes,. *Nat. Energy* **2018**, *3*, 739−746.

(38) Xu, K. Nonaqueous Liquid Electrolytes for Lithium-Based Rechargeable Batteries,. *Chemical Reviews* **2004**, *104*, 4303.

(39) Xia, Y.; Fujieda, T.; Tatsumi, K.; Prosini, P. P.; Sakai, T. Thermal and electrochemical stability of cathode materials in solid polymer electrolyte,. *J. Power Sources* **2001**, *92* (1−2), 234−243.

https://doi.org/10.1021/acsomega.3c03081
ACS Omega 2023, 8, 36753−36763

(40) Boisset, A.; Menne, S.; Jacquemin, J.; Balducci, A.; Anouti, M. Deep eutectic solvents based on N-methylacetamide and a lithium salt as suitable electrolytes for lithium-ion batteries,. *Phys. Chem. Chem. Phys.* **2013**, *15* (46), 20054−20063.
(41) Boisset, A.; Jacquemin, J.; Anouti, M. Physical properties of a new Deep Eutectic Solvent based on lithium bis[(trifluoromethyl)-sulfonyl]imide and N-methylacetamide as superionic suitable electrolyte for lithium ion batteries and electric double layer capacitors,. *Electrochim. Acta* **2013**, *102*, 120−126.
(42) Ratner, M. A.; Johansson, P.; Shriver, D. F. Polymer electrolytes: Ionic transport mechanisms and relaxation coupling,. *MRS Bull.* **2000**, *25* (3), 31−37.
(43) Agrawal, R. C.; Pandey, G. P. Solid polymer electrolytes: Materials designing and all-solid-state battery applications: An overview,. *J. Phys. D. Appl. Phys.* **2008**, *41* (22), 223001.
(44) Zheng, J.; Lochala, J. A.; Kwok, A.; Deng, Z. D.; Xiao, J. Research Progress towards Understanding the Unique Interfaces between Concentrated Electrolytes and Electrodes for Energy Storage Applications,. *Adv. Sci.* **2017**, *4* (8), 1700032.
(45) Hu, Y.; Li, H.; Huang, X.; Chen, L. Novel room temperature molten salt electrolyte based on LiTFSI and acetamide for lithium batteries,. *Electrochem. commun.* **2004**, *6* (1), 28−32.
(46) Qiu, J.; Liu, X.; Chen, R.; Li, Q.; Wang, Y.; Chen, P.; Gan, L.; Lee, S.; Nordlund, D.; Liu, Y.; et al. Enabling Stable Cycling of 4.2 V High-Voltage All-Solid-State Batteries with PEO-Based Solid Electrolyte,. *Adv. Funct. Mater.* **2020**, *30* (22), 1909392.
(47) Li, Z.; Zhao, Y.; Tenhaeff, W. E. Determining the Absolute Anodic Stability Threshold of Polymer Electrolytes: A Capacity-Based Electrochemical Method,. *Chem. Mater.* **2021**, *33* (6), 1927−1934.
(48) Hernández, G.; Johansson, I. L.; Mathew, A.; Sångeland, C.; Brandell, D.; Mindemark, J. Going Beyond Sweep Voltammetry: Alternative Approaches in Search of the Elusive Electrochemical Stability of Polymer Electrolytes,. *Journal of The Electrochemical Society* **2021**, *168*, 100523.
(49) De Sloovere, D.; Vanpoucke, D. E. P.; Paulus, A.; Joos, B.; Calvi, L.; Vranken, T.; Reekmans, G.; Adriaensens, P.; Eshraghi, N.; Mahmoud, A.; et al. Deep Eutectic Solvents as Nonflammable Electrolytes for Durable Sodium-Ion Batteries,. *Adv. Energy Sustain. Res.* **2022**, *3*, 2100159.
(50) Brouillette, D.; Irish, D. E.; Taylor, N. J.; Perron, G.; Odziemkowski, M.; Desnoyers, J. E. Stable solvates in solution of lithium bis(trifluoromethylsulfone)imide in glymes and other aprotic solvents: Phase diagrams, crystallography and Raman spectroscopyElectronic supplementary information (ESI) available: Crystallographic data (single crystal data) in cif format (CCDC reference number 184345). See http://www.rsc.org/suppdata/cp/b2/b203776a/. *Phys. Chem. Chem. Phys.* **2002**, *4* (24), 6063−6071.
(51) Miyazawa, T.; Shimanouchi, T.; Mizushima, S. i. Normal Vibrations of N-Methylacetamide,. *J. Chem. Phys.* **2004**, *29* (3), 611−616.
(52) Janek, J.; Zeier, W. G. A solid future for battery development. *Nature Energy*; Nature Publishing Group, 2016; Vol. *1*, pp 1−4, Sep. 08, no. 9.
(53) Khurana, R.; Schaefer, J. L.; Archer, L. A.; Coates, G. W. Suppression of Lithium Dendrite Growth Using Cross-Linked Polyethylene/Poly(ethylene oxide) Electrolytes: A New Approach for Practical Lithium-Metal Polymer Batteries,. *J. Am. Chem. Soc.* **2014**, *136*, 7395−7402.
(54) Tran, M. K.; Rodrigues, M. T. F.; Kato, K.; Babu, G.; Ajayan, P. M. Deep eutectic solvents for cathode recycling of Li-ion batteries,. *Nat. Energy* **2019**, *4* (4), 339−345.
(55) Zhang, X.; Jiang, W. J.; Mauger, A.; Qilu; Gendron, F.; Julien, C. M. Minimization of the cation mixing in Li1+x(NMC)1-xO2 as cathode material,. *J. Power Sources* **2010**, *195* (5), 1292−1301.
(56) Sun, G.; Yin, X.; Yang, W.; Song, A.; Jia, C.; Yang, W.; Du, Q.; Ma, Z.; Shao, G. The effect of cation mixing controlled by thermal treatment duration on the electrochemical stability of lithium transition-metal oxides,. *Phys. Chem. Chem. Phys.* **2017**, *19* (44), 29886−29894.
(57) Yusim, Y.; Trevisanello, E.; Ruess, R.; Richter, F. H.; Mayer, A.; Bresser, D.; Passerini, S.; Janek, J.; Henss, A. Evaluation and Improvement of the Stability of Poly(ethylene oxide)-based Solid-state Batteries with High-Voltage Cathodes,. *Angew. Chemie Int. Ed.* **2023**, *62*, No. e202218316.
(58) Rey, I.; Johansson, P.; Lindgren, J.; Lassègues, J. C.; Grondin, J.; Servant, L. Spectroscopic and Theoretical Study of (CF3SO2)2N-(TFSI-) and (CF3SO2)2NH (HTFSI),. *J. Phys. Chem. A* **1998**, *102* (19), 3249−3258.
(59) Hu, Y.; Wang, Z.; Li, H.; Huang, X.; Chen, L. Spectroscopic and DFT studies to understand the liquid formation mechanism in the LiTFSI/acetamide complex system,. *Spectrochim. Acta Part A Mol. Biomol. Spectrosc.* **2005**, *61* (9), 2009−2015.
(60) Lassègues, J. C.; Grondin, J.; Aupetit, C.; Johansson, P. Spectroscopic identification of the lithium ion transporting species in LiTFSI-doped ionic liquids,. *J. Phys. Chem. A* **2009**, *113* (1), 305−314.
(61) Lim, H. D.; Park, J. H.; Shin, H. J.; Jeong, J.; Kim, J. T.; Nam, K. W.; Jung, H. G.; Chung, K. Y. A review of challenges and issues concerning interfaces for all-solid-state batteries,. *Energy Storage Mater.* **2020**, *25*, 224−250.

https://doi.org/10.1021/acsomega.3c03081
ACS Omega 2023, 8, 36753−36763